remote sensing

MDPI

Article

Thorough Understanding and 3D Super-Resolution Imaging for Forward-Looking Missile-Borne SAR via a Maneuvering Trajectory

Tong Gu [1], Yifan Guo [2,*], Chen Zhao [3], Jian Zhang [4], Tao Zhang [5] and Guisheng Liao [1]

[1] Academy of Advanced Interdisciplinary Research, Xidian University, Xi'an 710071, China; gutong02@xidian.edu.cn (T.G.); liaogs@xidian.edu.cn (G.L.)
[2] School of Marine Science and Technology, Northwestern Polytechnical University, Xi'an 710071, China
[3] State Key Laboratory of Millimeter Wave, Beijing Institute of Remote Sensing Equipment, Beijing 100080, China; zhaochen212930304@126.com
[4] Tianjin Jinhang Institute of Technical Physics, Tianjin 300300, China; zhangjian8358@tjjh.com
[5] AVIC LEIHUA Electronic Technology Research Institute, Wuxi 214063, China; tslnzhangtao@163.com
* Correspondence: yifanguo@stu.xidian.edu.cn

Abstract: For missile-borne platforms, traditional SAR technology consistently encounters two significant shortcomings: geometric distortion of 2D images and the inability to achieve forward-looking imaging. To address these issues, this paper explores the feasibility of using a maneuvering trajectory to enable forward-looking and three-dimensional imaging by analyzing the maneuvering characteristics of an actual missile-borne platform. Additionally, it derives the corresponding resolution characterization model, which lays a theoretical foundation for future applications. Building on this, the paper proposes a three-dimensional super-resolution imaging algorithm that combines axis rotation with compressed sensing. The axis rotation not only realizes the dimensionality reduction of data, but also can expand the observation scenario in the cross-track dimension. The proposed algorithm first focuses on the track-vertical plane to extract 2D position parameters. Then, a compressed sensing-based process is applied to extract reflection coefficients and super-resolution cross-track position parameters, thereby achieving precise 3D imaging reconstruction. Finally, numerical simulation results confirm the effectiveness and accuracy of the proposed algorithm.

Keywords: maneuvering; forward-looking; three-dimensional imaging; axis rotation; compress sensing; super-resolution

Citation: Gu, T.; Guo, Y.; Zhao, C.; Zhang, J.; Zhang, T.; Liao, G. Thorough Understanding and 3D Super-Resolution Imaging for Forward-Looking Missile-Borne SAR via a Maneuvering Trajectory. *Remote Sens.* **2024**, *16*, 3378. https://doi.org/10.3390/rs16183378

Academic Editor: Dusan Gleich

Received: 31 July 2024
Revised: 29 August 2024
Accepted: 6 September 2024
Published: 11 September 2024

1. Introduction

Thanks to the ability to provide high-resolution microwave imagery of the observed area regardless of weather conditions, synthetic aperture radar (SAR) [1–4] has become one of the most attractive radar techniques. Meanwhile, with the rapid development of electronic technology and the miniaturization of components in recent years, missile-borne SAR has become possible. However, different from traditional side-looking SAR, missile-borne SAR [5–7] often requires the antenna to present a large squint observation angle in order to detect longer distances and a forward target. Further, various algorithms have been proposed to solve the above requirements, such as time domain algorithms [8,9] (back-projection algorithm (BPA) and the fast factorized back-projection algorithm (FFBPA), etc.) and frequency domain algorithms [10–18] (Range–Doppler algorithm (RDA), Chirp Scaling algorithm, Nonlinear Chirp Scaling algorithm (NCSA) and Frequency Scaling algorithm (FSA), etc.). Nevertheless, both the geometric model and the imaging algorithm of the above missile-borne SAR entail 2D imaging detection through traditional linear trajectory, the limitations of which are twofold, as follows: the geometric distortion of 3D object on 2D images; the large squint cannot detect the front object. For solving these issues, the concept of 3D forward-looking imaging has gained the attention of scholars.

For achieving 3D forward-looking imaging detection, the primary task is to solve the issue of a missing aperture compared to traditional SAR. To date, there are two main ways to complete the aperture: Firstly, multi-channel interference [19–26], such as TomoSAR, HoloSAR and Linear array SAR, which has no requirements for the flight trajectory of the platform, but needs to be able to form a large aperture antenna. However, due to the limited volume of the missile platform, the above technical approaches are difficult to apply. Secondly, trajectory deviation [27–33], such as CSAR, CLSAR. Their principle is to form the third dimensional aperture through the trajectory, thereby achieving 3D object detection. From the technical point of view, it is more suitable for the missile platform, but the trajectory deviation of the above technical approach is concentrated in the plane and does not involve the research and analysis of 3D deviation similar to the missile platform. Following the second technical idea and combining it with an actual ballistic study, a novel 3D forward-looking super-resolution imaging method for missile-borne SAR via maneuvering trajectory is proposed, in which we first validate the feasibility of using maneuvering trajectory for 3D forward-looking through multiple actual ballistic data, and then the 3D resolution is derived, including an analysis of the influence of different parameters on the 3D resolution. Based on this, an effective 3D forward-looking imaging algorithm is proposed, which consist of two steps: axis rotation and super-resolution extraction through compressed sensing [34–40]. The operation of axis rotation is used to widen the observation scenario, thereby extracting the position parameter of the vertical and track dimension. Then, compressed sensing is applied to extract the reflection coefficient and cross-track position. Finally, the 3D image will be reconstructed effectively.

This paper is organized as follows: Section 2 assesses the feasibility of using maneuvering trajectory for the 3D forward-looking approach through multiple actual ballistics, and then analyzes its 3D resolution in detail; Section 3 describes a 3D forward-looking super-resolution imaging algorithm, combining axis rotation and compressed sensing; Section 4 further tests the proposed algorithm through several simulation experiments. Finally, summations of the whole paper are provided in Section 5.

2. The Understanding of Maneuvering Trajectory for Three-Dimensional and Forward-Looking Missile-Borne SAR

As illustrated in Figure 1, we here simulate multiple actual ballistic trajectories (note that the data source cannot be disclosed). Each trajectory exhibits a significant deviation arc caused by ballistic maneuvers, and these maneuvering paths are typically underutilized during the guidance process. Given this, we are exploring the potential value of these trajectories. From Figure 1b,c, it is evident that the maneuvering trajectories include pull deviations in the X-cross-track, Y-track, and Z-vertical dimensions. From a detection standpoint, this implies three-dimensional degrees of freedom/apertures, which could enable the possibility of three-dimensional target detection. To further clarify this, we also provide the aperture size of the maneuvering trajectories in the standard coordinate system, as shown in Table 1. It is clear from these data that utilizing these maneuvering trajectories for three-dimensional imaging detection is indeed feasible.

Table 1. The 3D trajectory drop of multiple simulated actual ballistics.

Ballistic	Trajectory Drop-X	Trajectory Drop-Y	Trajectory Drop-Z
trajectory 1	32,910 m	54,860 m	22,370 m
trajectory 2	9060 m	79,400 m	2440 m
trajectory 3	16,490 m	93,000 m	15,710 m
trajectory 4	34,272 m	82,530 m	34,070 m

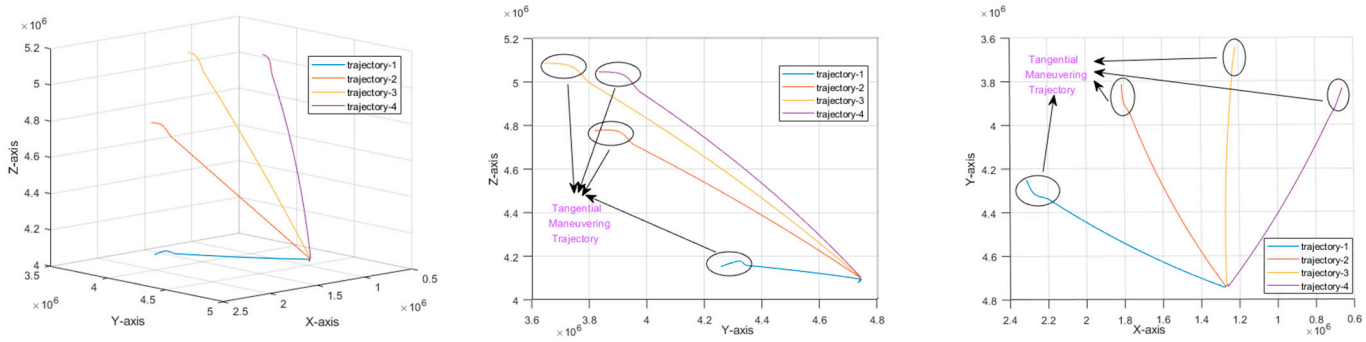

(**a**) (**b**) (**c**)

Figure 1. Multiple simulated actual ballistics. (**a**) The 3D spatial trajectory of ballistics. (**b**) The 2D profile trajectory of ballistics in the Y–Z plane. (**c**) The 2D profile trajectory of ballistics in the X–Y plane.

Using the parameters in Table 1, we analyze the changes in the view angle between the observation angle and the target along the maneuvering trajectory segment. Typically, an angle within a range of plus or minus 5 degrees is considered to fall within the forward-looking category. As shown in Figure 2, the overall angle change caused by the maneuvering trajectory remains within 3 degrees, with a slight reduction in the later stages due to the trajectory maneuvering back. In summary, it can be concluded that this maneuvering trajectory enables both forward-looking and 3D imaging simultaneously, offering a distinct advantage over the traditional large squint SAR mode.

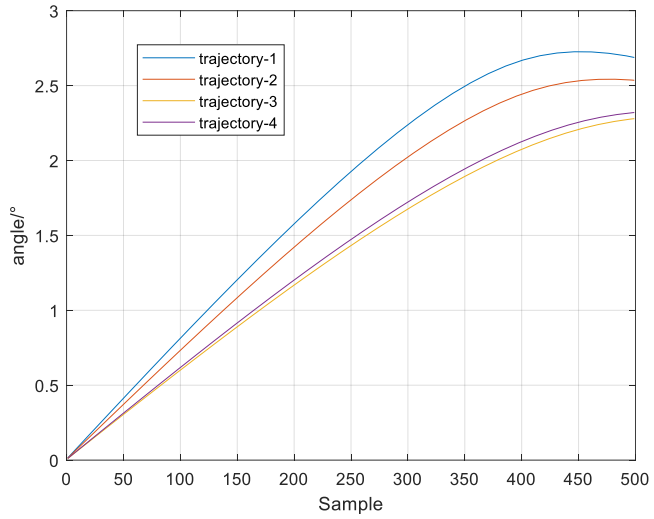

Figure 2. The angle change caused by maneuvering trajectory.

After completing the feasibility analysis of three-dimensional forward-looking imaging, another crucial factor to consider is the resolution capability afforded by the maneuvering trajectory, as this directly determines its practical application potential. For simplicity, we assume the target is located at the origin, and the position coordinates of the missile platform at the $i-$th slow time are (x_i, y_i, z_i). The pitch and azimuth angles from the missile platform relative to the target are denoted as $\varphi(t_i)$ and $\theta(t_i)$, respectively. Thus, the vector representation of the line between the target and the platform can be expressed as

$$\mathbf{r}(\varphi(\tau_i), \theta(\tau_i)) = r_i \begin{bmatrix} \cos(\varphi(\tau_i))\cos(\theta(\tau_i)) \\ \cos(\varphi(\tau_i))\sin(\theta(\tau_i)) \\ \sin(\varphi(\tau_i)) \end{bmatrix} \tag{1}$$

in which $r_i = \sqrt{x_i^2 + y_i^2 + z_i^2}$. Assuming that the radar system sends broadband linear frequency modulation signals and processes them with dechirp, then the echo signal can be written as

$$S(\tau_i, \theta_i, \varphi_i) = rect\left(\frac{t - 2\mathbf{r}_i/c}{T_p}\right)\exp(-jk\mathbf{r}_i) \tag{2}$$

where $k = 4\pi(f_c + \gamma t)/c$ (f_c is the center frequency, γ is the frequency modulation rate and c is the light speed). Define $\Omega(\tau_i, \varphi_i, \theta_i) = k\mathbf{r}_i$ as the phase history of signal echo propagation; then, its spatial frequencies at the standard wavenumber spectrum geometry—$\mathbf{k_x}$-$\mathbf{k_y}$-$\mathbf{k_z}$, as shown in Figure 3—are as follows:

$$\begin{aligned} k_x &= \frac{\partial\Omega}{\partial x} = k\cos(\varphi(\tau_i))\cos(\theta(\tau_i)) \\ k_y &= \frac{\partial\Omega}{\partial y} = k\cos(\varphi(\tau_i))\sin(\theta(\tau_i)) \\ k_z &= \frac{\partial\Omega}{\partial z} = k\sin(\varphi(\tau_i)) \end{aligned} \tag{3}$$

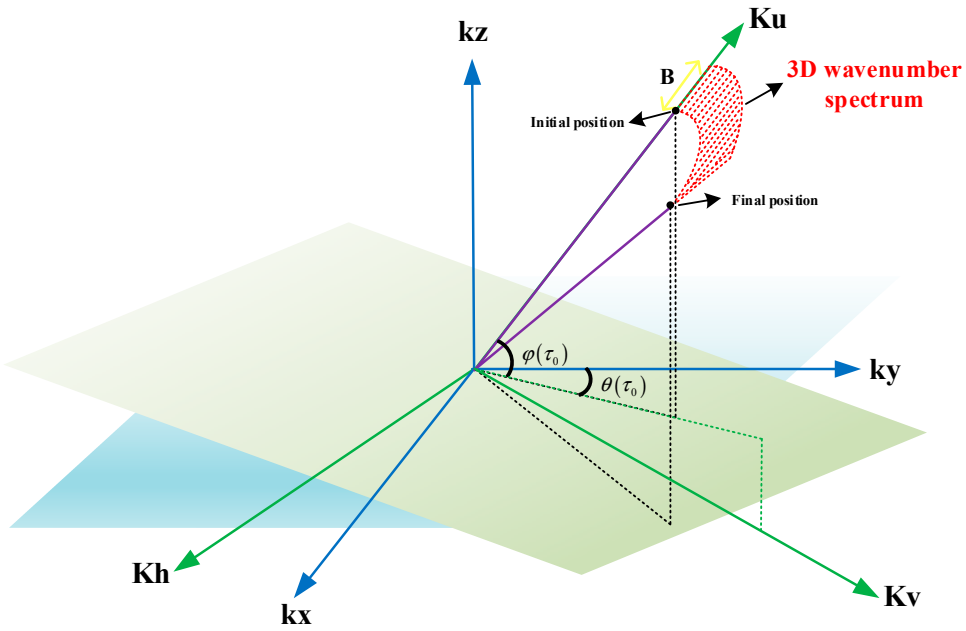

Figure 3. Wavenumber spectrum geometry, in which $\mathbf{k_x}$-$\mathbf{k_y}$-$\mathbf{k_z}$ denotes the standard wavenumber spectrum geometry and **Kh-Kv-Ku** denotes the wavenumber spectrum geometry along the line of sight direction. In addition, the green and blue squares correspond to the **Kh-Kv** plane and $\mathbf{k_x}$-$\mathbf{k_y}$ plane, respectively.

In theory, its 3D resolution corresponds to the wavenumber spectrum widths projected on the $\mathbf{k_x}$, $\mathbf{k_y}$ and $\mathbf{k_z}$ axes, that is,

$$\begin{aligned} \delta_{kx} &= c/2/[\max(k_x) - \min(k_x)] \\ \delta_{ky} &= c/2/[\max(k_y) - \min(k_y)] \\ \delta_{kz} &= c/2/[\max(k_z) - \min(k_z)] \end{aligned} \tag{4}$$

However, it is relatively difficult to solve Formula (4) directly due to the irregular, asymmetric and non-straight maneuvering trajectory. Therefore, we give an alternative—**Kh-Kv-Ku**, as shown in Figure 3, which is established based on the maneuvering trajectory. The advantage of this coordinate system design is that it allows for the detailed calculation of resolution based on the actual ballistic trajectory. Here, we assume that the azimuth angle and pitch angle at the initial time of maneuvering trajectory are $\theta(\tau_0)$ and $\varphi(\tau_0)$. Then,

the **Kh-Kv-Ku** coordinate system can be realized by rotating $\theta(\tau_0)$ along the $\mathbf{k_z}$ axis and $\pi/2 - \varphi(\tau_0)$ along the $\mathbf{k_x}$ axis, respectively. The red grid area denotes the 3D wavenumber spectrum, which begins at the initial time of the maneuvering trajectory and ends at the end of the maneuvering trajectory on the horizontal plane. The width is determined by the bandwidth $B = \gamma \cdot T_p$ of the transmitted signal. Based on the above coordinate system design, we define the range dimension by the line-of-sight at initial time, and the normalized **Ku** axis can be written as (Λ notes the normalized operation)

$$\overset{\Lambda}{\mathbf{Ku}} = [\cos(\varphi(\tau_0))\cos(\theta(\tau_0)), \cos(\varphi(\tau_0))\sin(\theta(\tau_0)), \sin(\varphi(\tau_0))] \tag{5}$$

At this moment, the projection of the wavenumber spectrum along the **Ku** axis can be easily calculated, as follows:

$$B_{Ku} = \max\left\{\frac{4\pi(f_c + B)}{c}\overset{\Lambda}{\mathbf{Ku}} \times \begin{bmatrix}\cos(\varphi(\tau_k))\cos(\theta(\tau_k))\\ \cos(\varphi(\tau_k))\sin(\theta(\tau_k))\\ \sin(\varphi(\tau_k))\end{bmatrix}\right\} - \min\left\{\frac{4\pi f_c}{c}\overset{\Lambda}{\mathbf{Ku}} \times \begin{bmatrix}\cos(\varphi(\tau_l))\cos(\theta(\tau_l))\\ \cos(\varphi(\tau_l))\sin(\theta(\tau_l))\\ \sin(\varphi(\tau_l))\end{bmatrix}\right\} \tag{6}$$

where k, $l(k, l = 1, 2, \cdots, N)$ is the $k/l-$th sampling position of the maneuvering trajectory. Form Formula (6), we can infer the value of B_{Ku} in advance, while the maneuvering trajectory is determined. Then, the resolution can be written as

$$\delta_{Ku} = \frac{c}{2B_{Ku}} \tag{7}$$

Furthermore, Figure 4 gives the projection of the wavenumber spectrum along the **Kh** and **Kv** axis, and the definition of normalized **Kh** axis can be written as

$$\overset{\Lambda}{\mathbf{Kh}} = [\sin(\theta(\tau_0)), -\cos(\theta(\tau_0)), 0] \tag{8}$$

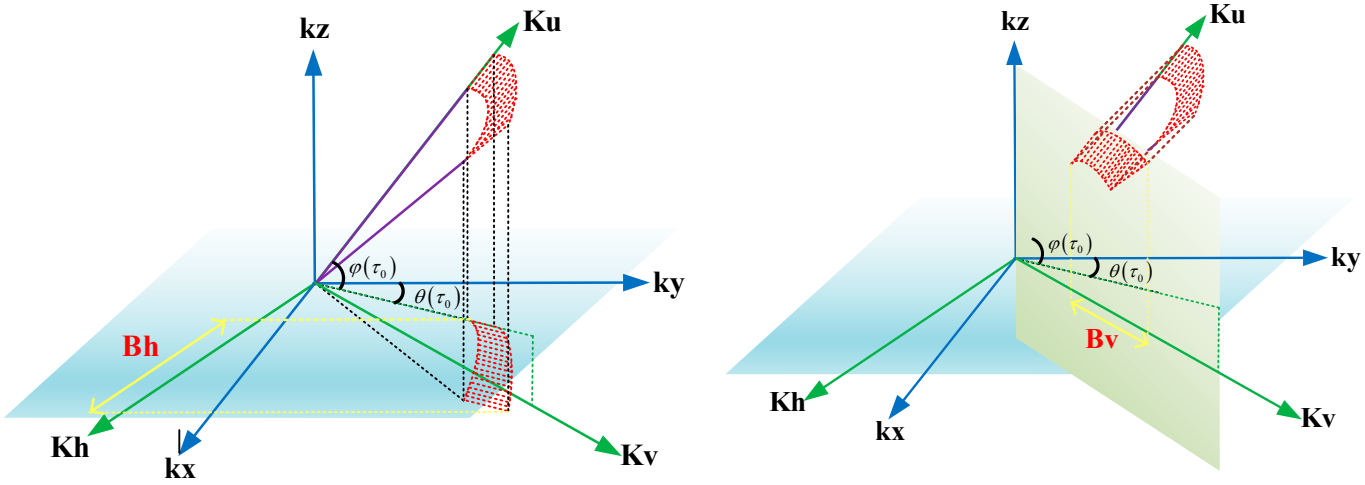

(**a**) (**b**)

Figure 4. The wavenumber spectrum projection geometry. (**a**) The projection along the **Kh** axis, in which the blue square correspond to $\mathbf{k_x}$-$\mathbf{k_y}$ plane; (**b**) the projection along the **Kv** axis, in which the green and blue squares correspond to the kz-Kv plane and kx-ky plane, respectively.

As shown in Figure 4a, we first project the wavenumber spectrum onto the $\mathbf{k_x}$-$\mathbf{k_y}$ plane with the range of value being $[\left[4\pi f_c \cos(\varphi(\tau_i))/c, 4\pi(f_c + B)\cos\left(\varphi\left(\tau_j\right)\right)/c\right], i, j = 1, 2, \cdots, N]$, and then project it vertically onto the **Kh** axis. So, the bandwidth on the **Kh** axis can be written as

$$B_{Kh} = \max\left\{\frac{4\pi(f_c+B)}{c}\cos(\varphi(\tau_k))\sin(\theta(\tau_k)-\theta_0)\right\} - \min\left\{\frac{4\pi f_c}{c}\cos(\varphi(\tau_l))\sin(\theta(\tau_l)-\theta_0)\right\} \tag{9}$$

where θ_0 is the azimuth angle at the initial time. Similarly, Figure 4b gives the process of projection onto the **Kv** axis, and its bandwidth can be written as

$$\begin{aligned} B_{Kv} = &\max\left\{\tfrac{4\pi(f_c+B)}{c}\sqrt{1-\cos(\varphi(\tau_k))^2\sin(\theta(\tau_k)-\theta_0)^2}\cdot\sin(\varphi_0-\varphi_{new\_k})\right\} \\ &-\min\left\{\tfrac{4\pi f_c}{c}\sqrt{1-\cos(\varphi(\tau_l))^2\sin(\theta(\tau_l)-\theta_0)^2}\cdot\sin(\varphi_0-\varphi_{new\_l})\right\} \end{aligned} \tag{10}$$

where φ_0 is the pitch angle at the initial time and the definition of φ_{new} is

$$\varphi_{new} = a\sin\frac{\sin(\varphi(\tau))}{\sqrt{1-\cos(\varphi(\tau))^2\sin(\theta(\tau)-\theta_0)}} \tag{11}$$

Based on the above analysis, we can determine the 3D resolution of the rotated **Ku-Kh-Kv** coordinate system. This resolution can also be used to calculate the 3D resolution in the standard coordinate system, as follows:

$$\begin{bmatrix} B_{kx} \\ B_{ky} \\ B_{kz} \end{bmatrix} = \begin{bmatrix} \cos\varphi_0\cos\theta_0 & \sin\theta_0 & \sin\varphi_0\cos\theta_0 \\ \cos\varphi_0\sin\theta_0 & -\cos\theta_0 & \sin\varphi_0\sin\theta_0 \\ \sin\varphi_0 & 0 & -\cos\varphi_0 \end{bmatrix} \begin{bmatrix} B_{Ku} \\ B_{Kh} \\ B_{Kv} \end{bmatrix} \tag{12}$$

and

$$\begin{aligned} \delta_{kx} &\approx \tfrac{c}{2B_{kx}} = \tfrac{c}{2(B_{Ku}\cos\varphi_0\cos\theta_0+B_{Kv}\sin\varphi_0\cos\theta_0+B_{Kh}\sin\theta_0)} \\ \delta_{ky} &\approx \tfrac{c}{2B_{ky}} = \tfrac{c}{2(B_{Ku}\cos\varphi_0\sin\theta_0+B_{Kv}\sin\varphi_0\sin\theta_0-B_{Kh}\cos\theta_0)} \\ \delta_{kz} &\approx \tfrac{c}{2B_{kz}} = \tfrac{c}{2(B_{Ku}\sin\varphi_0-B_{Kv}\cos\varphi_0)} \end{aligned} \tag{13}$$

To validate the accuracy of the 3D resolution derived above, we use the simulation parameters listed in Table 1. Figure 5 illustrates the 3D envelope at the scenario center, demonstrating the feasibility of 3D imaging using the maneuvering trajectory. For this simulation, we selected maneuvering trajectory 2, with a center frequency of 40 GHz and a transmitting bandwidth of 400 MHz. A comparison between the estimated and actual values of 3D resolution is presented in Table 2, showing that the estimated values align closely with the true values. However, since the 3D resolution is fundamentally a multi-dimensional variable function influenced by factors such as center frequency, transmitting bandwidth, pitch angle, and azimuth angle, we further investigate the impacts of these parameters. Here, we define the ranges of center frequency, bandwidth, pitch angle, and azimuth angle as $[20\,\text{GHz} \sim 40\,\text{GHz}]$, $[200\,\text{MHz} \sim 800\,\text{MHz}]$, $[50^\circ, 80^\circ]$ and $[30^\circ, 60^\circ]$, respectively (note that while the angle range is broad, it will only apply to a small portion of this range in practice). Figure 6 illustrates the variation in 3D resolution. It can be observed that the 3D resolution is significantly influenced by bandwidth, increasing as both bandwidth and center frequency rise. From Figure 6a,d,g,j, we see that the resolution in the $\mathbf{k_z}$ dimension is less affected by azimuth angle, though its upper bound increases with a rising pitch angle. In the $\mathbf{k_x}$ dimension, as shown in Figure 6b,e,h,k, the upper bound of the resolution increases rapidly with the azimuth angle. Finally, Figure 6c,f,i,l indicate that the upper bound of the resolution in the $\mathbf{k_y}$ dimension is inversely proportional to the azimuth angle but directly proportional to the pitch angle.

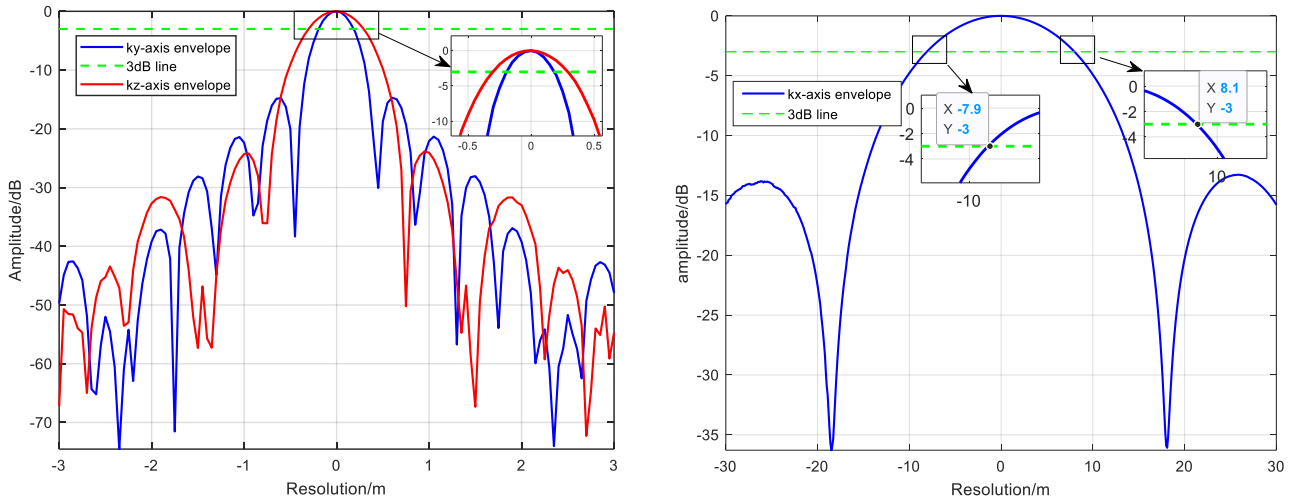

(**a**) (**b**)

Figure 5. 3D envelope of the scenario center. (**a**) The envelope of the $\mathbf{k_y}$ axis and $\mathbf{k_z}$ axis; (**b**) the envelope of the $\mathbf{k_x}$ axis.

Table 2. Detailed comparison of 3D resolution.

Resolution	$\mathbf{k_x}$/m	$\mathbf{k_y}$/m	$\mathbf{k_z}$/m
True value	16.25	0.588	0.425
Estimate value	16.23	0.574	0.440

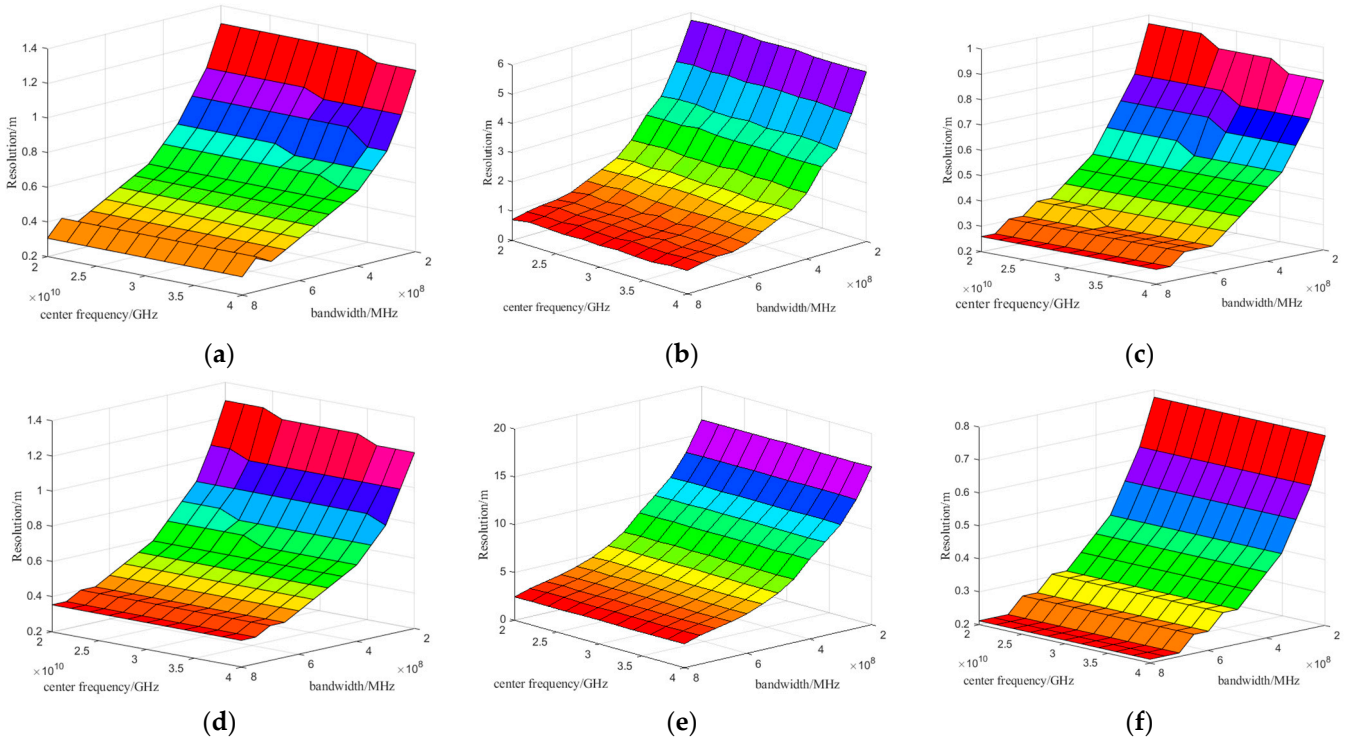

(**a**) (**b**) (**c**)

(**d**) (**e**) (**f**)

Figure 6. *Cont.*

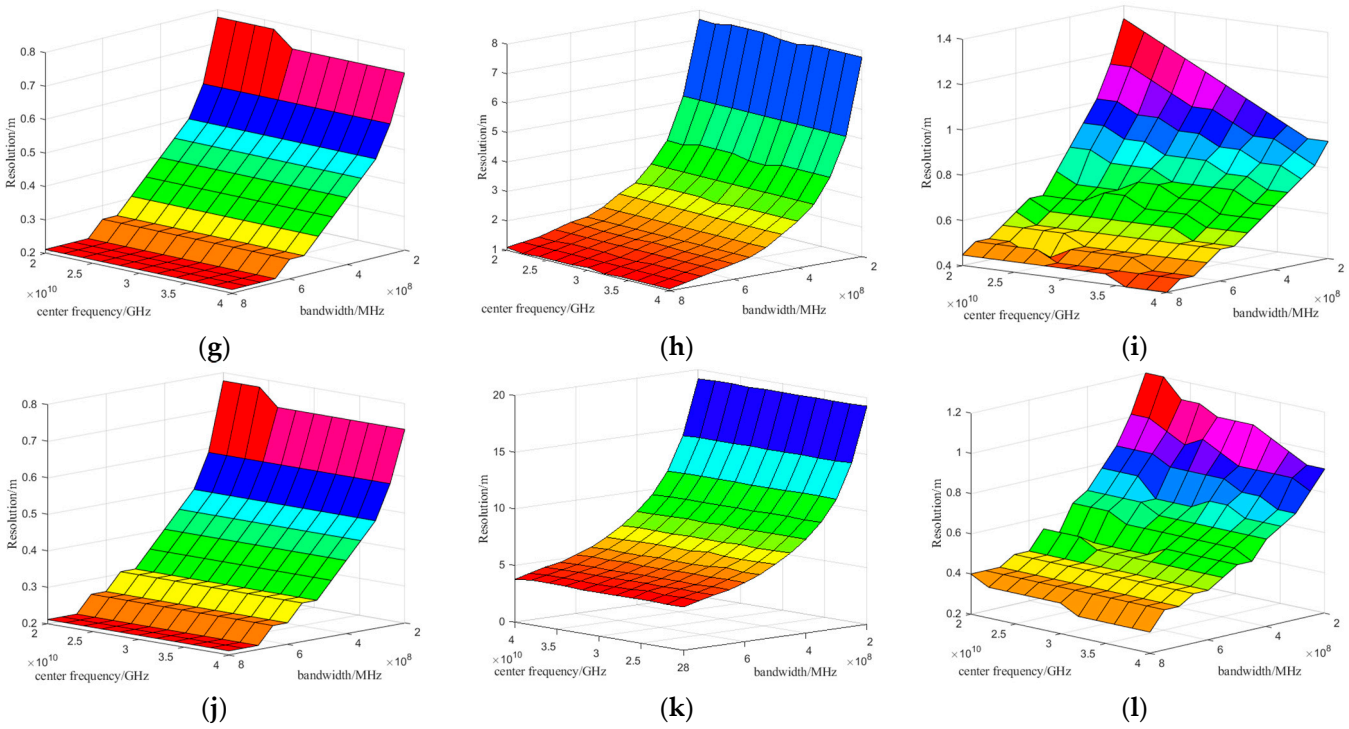

Figure 6. The influence analysis of center frequency, transmitting bandwidth, azimuth and pitch angle on the 3D resolution; (**a**) the $\mathbf{k_z}$ axis resolution with [30°, 50°]; (**b**) the $\mathbf{k_x}$ axis resolution with [30°, 50°]; (**c**) the $\mathbf{k_y}$ axis resolution with [30°, 50°]; (**d**) the $\mathbf{k_z}$ axis resolution with [30°, 80°]; (**e**) the $\mathbf{k_x}$ axis resolution with [30°, 80°]; (**f**) the $\mathbf{k_y}$ axis resolution with [30°, 80°]; (**g**) the $\mathbf{k_z}$ axis resolution with [60°, 50°]; (**h**) the $\mathbf{k_x}$ axis resolution with [60°, 50°]; (**i**) the $\mathbf{k_y}$ axis resolution with [60°, 50°]; (**j**) the $\mathbf{k_z}$ axis resolution with [60°, 80°]; (**k**) the $\mathbf{k_x}$ axis resolution with [60°, 80°]; (**l**) the $\mathbf{k_y}$ axis resolution with [60°, 80°].

In summary, we have demonstrated the feasibility of 3D forward-looking imaging using the maneuvering trajectory and conducted a detailed analysis of its resolution and influencing factors. The subsequent section will focus on the image processing methodology.

3. Three-Dimensional Super-Resolution Imaging Combining Axis Rotation and Compressed Sensing

Before proceeding with imaging processing, it is essential to first analyze the representation of the echo signal. Assuming the 3D scenario is discretized into uniform 3D grids-$\mathbf{\Omega} \in M \times N \times L$ and a linear frequency modulation signal is transmitted, the received echo signal, denoted as Formula (2), can be rewritten as:

$$\begin{aligned} S(\tau_i, \theta_i, \varphi_i) &= \int_{\mathbf{\Omega}} \delta_{\mathbf{\Omega}} \cdot rect\left(\frac{t - 2\mathbf{r}_i/c}{T_p}\right) \exp(-jk\mathbf{r}_i) \\ &= \int_{\mathbf{\Omega}} \delta_{\mathbf{\Omega}} \cdot rect\left(\frac{t - 2\mathbf{r}_i/c}{T_p}\right) \exp\left\{-jk\left(\begin{array}{l} x_{\mathbf{\Omega}} \cos(\varphi(\tau_i)) \cos(\theta(\tau_i)) \\ +y_{\mathbf{\Omega}} \cos(\varphi(\tau_i)) \sin(\theta(\tau_i)) + z_{\mathbf{\Omega}} \sin(\varphi(\tau_i)) \end{array}\right)\right\} \end{aligned} \tag{14}$$

where $\delta_{\mathbf{\Omega}}$ denotes the reflection coefficient of $\mathbf{\Omega}$. In order to get a more intuitive understanding of Formula (14), we perform matrix processing on it, as follows:

$$
\begin{aligned}
&Define: \\
&\boldsymbol{\alpha}_i = \begin{bmatrix} \exp\{-jk(x_1\cos(\varphi(\tau_i))\cos(\theta(\tau_i)))\} \\ \exp\{-jk(x_2\cos(\varphi(\tau_i))\cos(\theta(\tau_i)))\} \\ \vdots \\ \exp\{-jk(x_M\cos(\varphi(\tau_i))\cos(\theta(\tau_i)))\} \end{bmatrix} \boldsymbol{\beta}_i = \begin{bmatrix} \exp\{-jk(y_1\cos(\varphi(\tau_i))\sin(\theta(\tau_i)))\} \\ \exp\{-jk(y_2\cos(\varphi(\tau_i))\sin(\theta(\tau_i)))\} \\ \vdots \\ \exp\{-jk(y_N\cos(\varphi(\tau_i))\sin(\theta(\tau_i)))\} \end{bmatrix} \\
&\boldsymbol{\chi}_i = \begin{bmatrix} \exp\{-jk(z_1\sin(\theta(\tau_i)))\} \\ \exp\{-jk(z_2\sin(\theta(\tau_i)))\} \\ \vdots \\ \exp\{-jk(z_L\sin(\theta(\tau_i)))\} \end{bmatrix} \qquad \boldsymbol{\Omega}_\delta = \begin{bmatrix} \delta(x_1,y_1,z_1),\delta(x_2,y_1,z_1),\cdots,\delta(x_M,y_1,z_1),\cdots, \\ \delta(x_1,y_N,z_L),\cdots,\delta(x_M,y_N,z_L) \end{bmatrix} \\
&\qquad\qquad \Downarrow \\
&\mathbf{S} = \mathbf{A}_{(K)\times(M\cdot N\cdot L)} = \begin{bmatrix} \boldsymbol{\alpha}_1\otimes\boldsymbol{\beta}_1\otimes\boldsymbol{\chi}_1 \\ \boldsymbol{\alpha}_2\otimes\boldsymbol{\beta}_2\otimes\boldsymbol{\chi}_2 \\ \cdots \\ \boldsymbol{\alpha}_K\otimes\boldsymbol{\beta}_K\otimes\boldsymbol{\chi}_K \end{bmatrix} \cdot \boldsymbol{\Omega}_\delta
\end{aligned} \tag{15}
$$

where $\otimes$ denotes the Kronecker product [41]. For Formula (15), there are two ways to solve it. One way is the time domain algorithm, such as BP, FBP or FFBP, which performs imaging through point by point compensation. However, it is time-consuming and inefficient. The other way involves solving a linear programming problem efficiently. However, the computational complexity of this method is primarily determined by the sampling ratio of $\boldsymbol{\Omega}$, which corresponds to the measurement matrix $\mathbf{A}$. If the size of $\mathbf{A}$ is too large, even traditional toolboxes become inefficient. So, can we combine these two approaches to reduce the size of $\mathbf{A}$ while also minimizing the 3D compensation required by the time domain algorithm?

To address this, we start by examining the wavenumber spectrum and its corresponding resolution. Figure 5 shows that the resolutions along $\mathbf{k_y}$ and $\mathbf{k_z}$ axes are at the sub-meter level, while that along the $\mathbf{k_x}$ axis is on the order of ten meters. This discrepancy is also evident from the wavenumber spectrum projection results in Figure 7. Based on these characteristics, we propose an efficient super-resolution imaging algorithm that utilizes FFBP to image the $\mathbf{k_y}$-$\mathbf{k_z}$ plane and compress sensing to achieve a super-resolution reconstructed along the $\mathbf{k_x}$ axis. However, this algorithm still faces a significant issue: the imaging area range along the $\mathbf{k_x}$ axis is equal to its theoretical resolution (i.e., the imaging area range is constrained by the $\mathbf{k_x}$ axis resolution, and the scatters with different $\mathbf{k_y}$/$\mathbf{k_z}$ positions within one $\mathbf{k_x}$ axis resolution unit will be focused at the same position). Consequently, once the spacing of any two scatters exceeds the $\mathbf{k_x}$ axis resolution, the false scatters may appear in the $\mathbf{k_y}$-$\mathbf{k}_z$ imaging plane. So, what can be done to alleviate this issue? In other words, how does one reduce the resolution of the $\mathbf{k_x}$ axis?

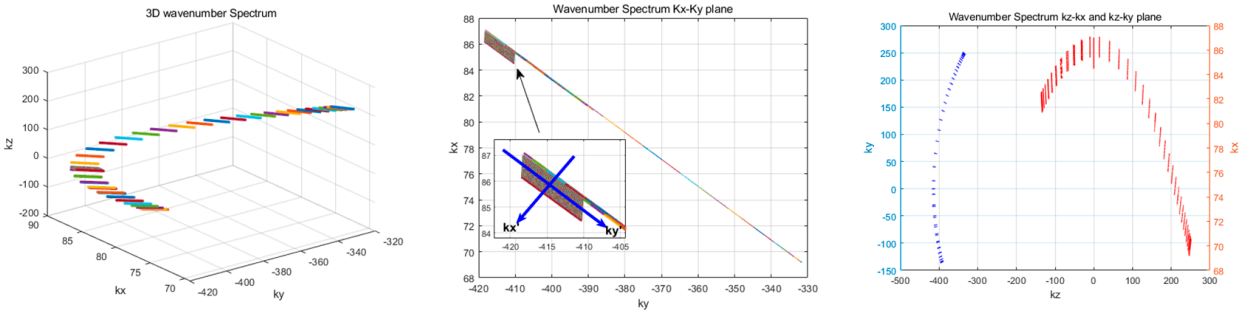

(**a**) (**b**) (**c**)

Figure 7. Wavenumber spectrum projection analysis of trajectory II. (**a**) 3D wavenumber spectrum. (**b**) $\mathbf{k_x}$-$\mathbf{k_y}$ wavenumber spectrum projection plane. (**c**) $\mathbf{k_z}$-$\mathbf{k_x}$ and $\mathbf{k_z}$-$\mathbf{k_y}$ wavenumber spectrum projection plane.

In order to solve this, we further analyze the wavenumber spectrum projection results. Upon closer inspection of Figure 7b, it becomes apparent that the projection bandwidth along the $\mathbf{k_x}$ axis is not minimal in the current $\mathbf{k_x}$-$\mathbf{k_y}$ axes definition. Therefore, we propose rotating the coordinate system to reduce the $\mathbf{k_x}$ axis resolution and broaden the range of the observation area. As illustrated in the inset of Figure 7b, we define new $\mathbf{k_x}'$-$\mathbf{k_y}'$ axes by rotating the $\mathbf{k_y}$ axis to align with the initial azimuth position (i.e., by rotating θ_0 with the $\mathbf{k_z}$ axis as the rotation axis). The projection bandwidth of the new coordinate system can then be expressed as follows:

$$\begin{bmatrix} B_{kx'} \\ B_{ky'} \\ B_{kz'} \end{bmatrix} = \begin{bmatrix} 0 & 1 & 0 \\ \cos\varphi_0 & 0 & \sin\varphi_0 \\ \sin\varphi_0 & 0 & -\cos\varphi_0 \end{bmatrix} \begin{bmatrix} B_{Ku} \\ B_{Kh} \\ B_{Kv} \end{bmatrix} \tag{16}$$

For verification, we select two scatters separated by 18 m along the $\mathbf{k_x}$ axis for verification. Figure 8a,b present a comparison of the 3D resolution, where the solid line corresponds to the standard coordinate system and the dashed line corresponds to the rotated co-ordinate system. Figure 8a indicates that the resolutions along the ($\mathbf{k_y}$, $\mathbf{k_z}$) and ($\mathbf{k_y}'$, $\mathbf{k_z}'$) axes are approximately the same, which aligns with the findings from the previous theoretical analysis in Formula (16). In contrast, Figure 8b illustrates that the resolution along the $\mathbf{k_x}$ axis is significantly smaller than that of the $\mathbf{k_x}'$ axis. Based on these conclusions, Figure 8c shows the $\mathbf{k_y}$-$\mathbf{k_z}$ and $\mathbf{k_y}'$-$\mathbf{k_z}'$ reconstructed plane. The $\mathbf{k_y}$-$\mathbf{k_z}$ reconstructed plane shows a false scatter due to the separation between the two scatters exceeding the resolution along the $\mathbf{k_x}$ aixs. However, the $\mathbf{k_y}'$-$\mathbf{k_z}'$ reconstructed plane eliminates the false scatter, indicating that the $\mathbf{k_x}'$ axis resolution is greater than the separation between the two scatters. Therefore, we can conclude that the coordinate system rotation approach is indeed feasible.

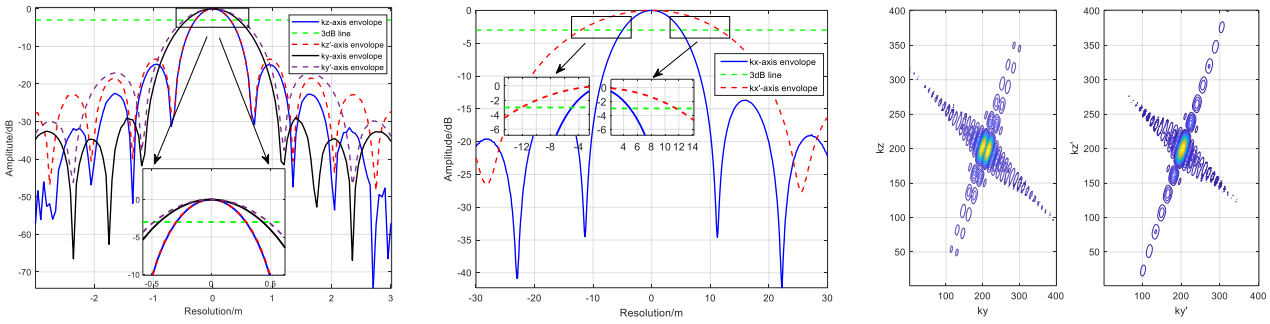

(**a**) (**b**) (**c**)

Figure 8. The 3D resolution verification after axis rotation. (**a**) The comparison between the $\mathbf{k_z}$/$\mathbf{k_y}$ axis and the $\mathbf{k_z}'$/$\mathbf{k_y}'$ axis. (**b**) The comparison between the $\mathbf{k_x}$ axis and $\mathbf{k_x}'$ axis. (**c**) The comparison between $\mathbf{k_y}$-$\mathbf{k_z}$ and $\mathbf{k_y}'$-$\mathbf{k_z}'$ focused plane.

After the $\mathbf{k_y}'$ and $\mathbf{k_z}'$ positions are extracted from the $\mathbf{k_y}'$-$\mathbf{k_z}'$ reconstructed plane, the next task is to get the $\mathbf{k_x}'$ positions of all scatters. As the $\mathbf{k_y}'$ and $\mathbf{k_z}'$ positions are known, the set $\mathbf{\Omega}$ will reduce to $M \times J$, and $J \ll N, L$ denotes the number of extracted positions. Therefore, both the measurement matrix $\mathbf{A}$ and reflection coefficient vector $\mathbf{\Omega}_\delta$ will achieve dimensionality reduction, and can be rewritten as

$$\begin{aligned} \mathbf{A}'_{K\times(M\times J\times J)} &= \left[\boldsymbol{\alpha}_1 \otimes (\boldsymbol{\beta}_1 \cdot \boldsymbol{\chi}_1), \boldsymbol{\alpha}_2 \otimes (\boldsymbol{\beta}_2 \cdot \boldsymbol{\chi}_2), \cdots, \boldsymbol{\alpha}_K \otimes (\boldsymbol{\beta}_K \cdot \boldsymbol{\chi}_K)\right]^T \\ \mathbf{\Omega}'_\delta &= \left[\delta(x_1, y_1, z_1), \delta(x_2, y_1, z_1), \cdots, \delta(x_M, y_1, z_1), \cdots, \delta\left(x_1, y_J, z_J\right), \cdots, \delta\left(x_M, y_J, z_J\right)\right] \\ &\Downarrow \\ \mathbf{S} &= \mathbf{A}' \cdot \mathbf{\Omega}'_\delta \end{aligned} \tag{17}$$

For Formula (17), we can convert it into the following typical linear programming problem [32]:

$$minimize\left\|\mathbf{A}' \cdot \mathbf{\Omega}'_{\delta} - \mathbf{S}\right\|_2^2 + \lambda\left\|\mathbf{\Omega}'_{\delta}\right\|_1 \quad (18)$$

where $\|\cdot\|_1$ denotes the L_1 norm and $\lambda > 0$ is the regularization parameter. To solve the Formula (18), high-quality implementations of the interior-point method including l1-magic [42] and PDCO [43] can be used, which utilize iterative algorithms, such as the conjugate gradients (CG) [44] or LSQR algorithm [45], to compute the search step. After applying compressed sensing, we obtain the reflection coefficients and positions of all scatters. Summarizing the entire processing procedure, the flowchart of the proposed dimension-reduction super-resolution 3D imaging algorithm is shown in Figure 9.

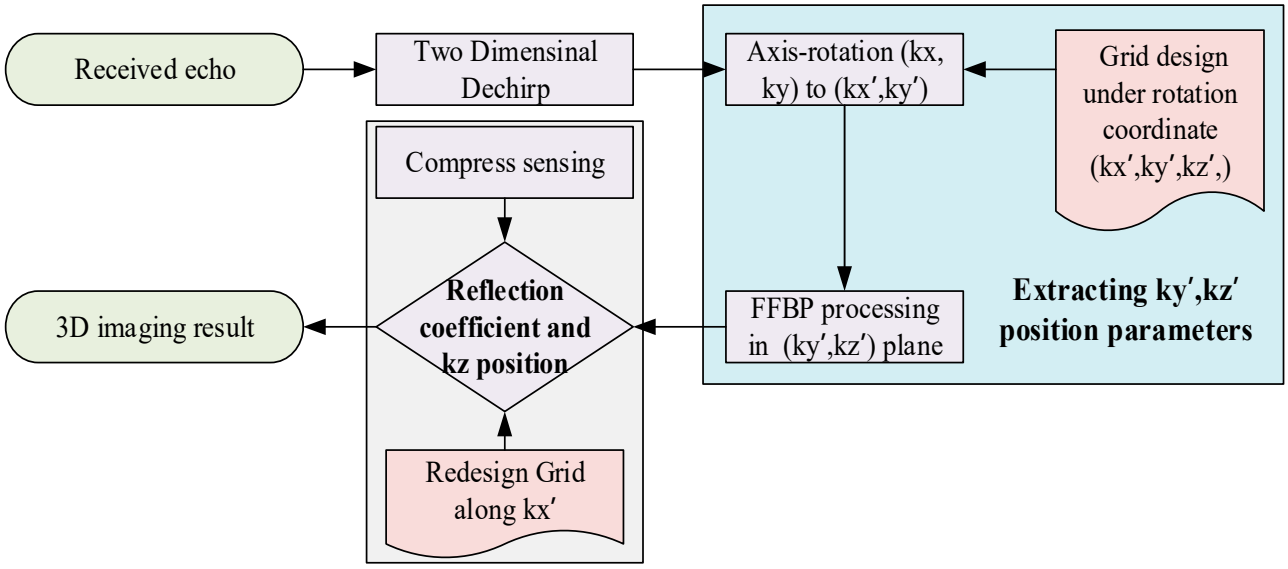

Figure 9. The flowchart of the proposed dimension-reduction super-resolution 3D imaging algorithm.

4. Simulation and Results

Here, we conduct the simulation verification in three steps. First, we verify the feasibility of the proposed 3D imaging algorithm using multiple scatters with both identical and varying reflection coefficients. Next, we explore the boundaries of the algorithm and examine the effects of signal-to-noise ratio and sampling rate on imaging performance. Finally, we validate the algorithm using point cloud models of actual complex target objects. It is important to note that the maneuvering trajectory II is used in all the simulations below.

4.1. 3D Imaging for Multi-Scatters with the Same and Varying Reflection Coefficients

To verify the feasibility of the proposed imaging algorithm, we not only present the final imaging results, but also demonstrate the corresponding parameter extraction process. First, consider Figure 10, where five scatters with varying reflection coefficients are depicted. Figure 10a,b show the $\mathbf{k_y}'$-$\mathbf{k_z}'$ positions and the $\mathbf{k_x}'$ positions, respectively. It is also evident that the vertical axis in Figure 10b corresponds to the reflection coefficients. In Figure 10a, it can be observed that the number of scatters is reduced to three. This reduction occurs because the three scatters distributed along the $\mathbf{k_x}'$ axis fall within a single $\mathbf{k_x}'$ axis resolution unit, causing them to overlap in the $\mathbf{k_y}'$-$\mathbf{k_z}'$ focused plane. To separate these three scatters, we apply compressed sensing to achieve super-resolution extraction, as shown in Figure 10b, where the five scatters reappear, and their $\mathbf{k_x}'$ positions and reflection coefficients are effectively extracted. Finally, the complete 3D imaging result and detailed comparisons are presented in Figure 10c and Table 3. Similarly, Figure 11 presents the 3D imaging process for seven scatters with identical reflection coefficients, with detailed comparisons shown in Table 4. Overall, both the 3D imaging and parameter comparison

results demonstrate that the proposed algorithm is a feasible and high-performance 3D imaging processing method for the maneuvering trajectory.

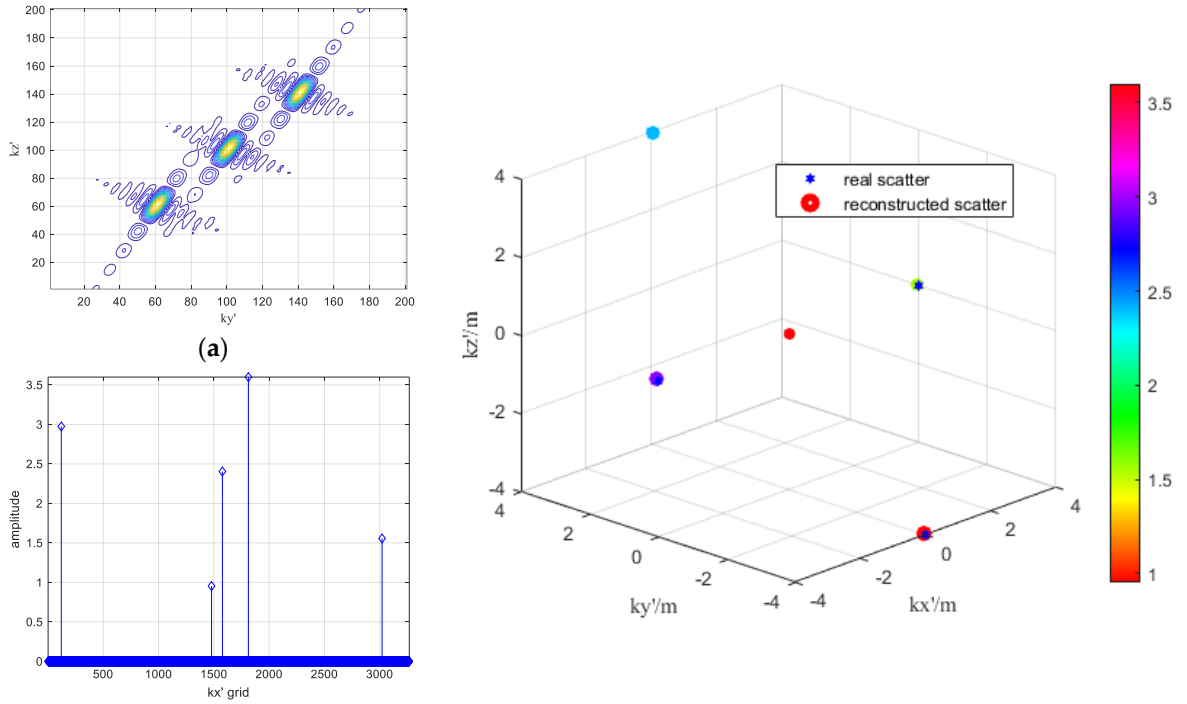

Figure 10. 3D imaging process of five scatters with varying reflection coefficients. (**a**) $\mathbf{k_y'}$-$\mathbf{k_z'}$ focused plane; (**b**) $\mathbf{k_x'}$-reflection coefficient extraction; (**c**) final 3D imaging result.

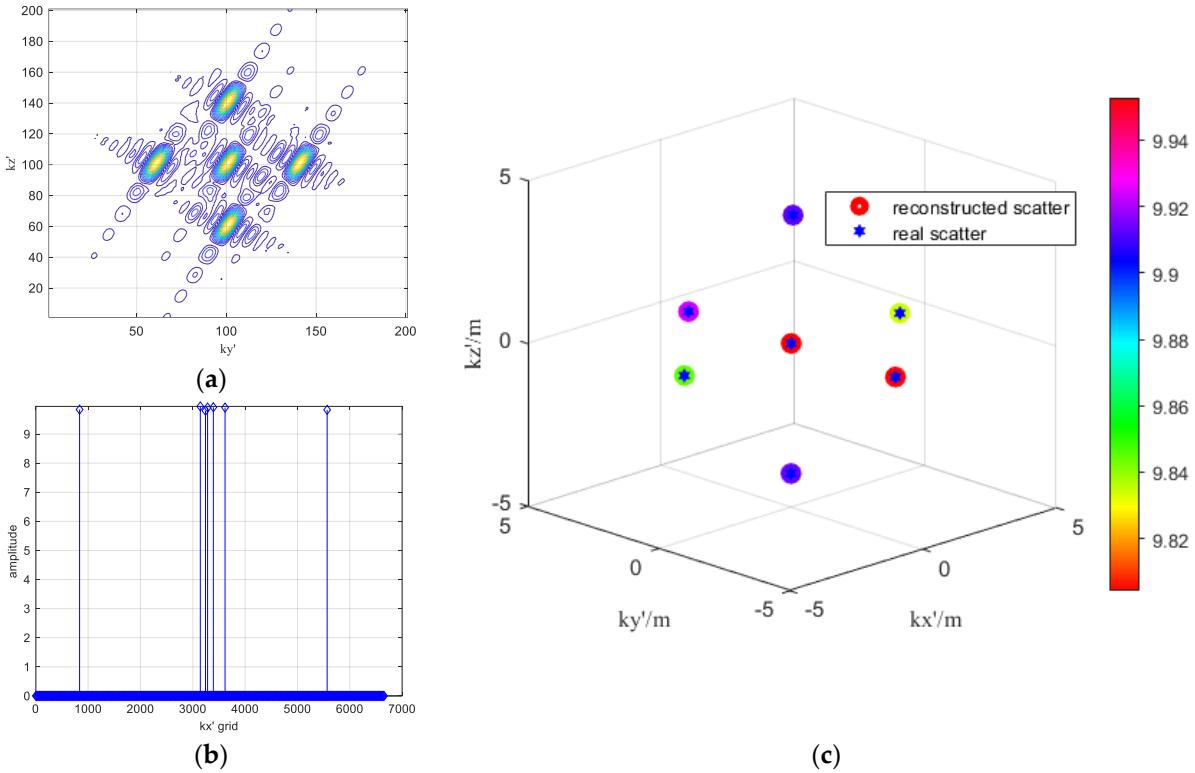

Figure 11. 3D imaging process of seven scatters with the same reflection coefficients. (**a**) $\mathbf{k_y'}$-$\mathbf{k_z'}$ focused plane; (**b**) $\mathbf{k_x'}$-reflection coefficient extraction; (**c**) final 3D imaging result.

Table 3. Detailed parameter comparison of five scatters with varying reflection coefficients.

Parameters	**Reflection Coefficients**					**3D Positions**				
True	1.00	2.40	3.60	1.60	3.00	(0, 0, 0)	(0, 4, 4)	(0, 4, −4)	(4, 0, 0)	(−4, 0, 0)
Reconstructed	0.948	2.40	3.578	1.558	2.973	(−0.02, 0, 0)	(0.10, 4, 4)	(−0.13, 4, −4)	(4.07, 0, 0)	(−4.05, 0, 0)

Table 4. Detailed parameter comparisons of seven scatters with same reflection coefficients.

Parameters	**Reflection Coefficients**							**3D Positions**						
True	10.00	10.00	10.00	10.00	10.00	10.00	10.00	(0, 0, 0)	(0, 4, 4)	(0, 4, −4)	(4, 0, 0)	(−4, 0, 0)	(0, 4, 0)	(0, −4, 0)
Reconstructed	9.83	9.94	9.81	9.93	9.93	9.90	9.86	(−0.02, 0, 0)	(0.10, 4, 4)	(−0.13, 4, −4)	(4.07, 0, 0)	(−4.05, 0, 0)	(0.05, 4, 0)	(−0.08, −4, 0)

4.2. Effects of the Signal-to-Noise Ratio and Sampling Rate on 3D Imaging Processing

Figure 12 illustrates the effects of signal-to-noise ratio (SNR) and sampling rate on 3D imaging processing, where real scatters are denoted by blue pentagrams and reconstructed scatters by red hexagons. The positions of the multi-scatters are referenced in Table 4. As shown in Figure 12a,d,g, the shapes of the multi-scatters are well reconstructed at a high sampling rate of M = 12,000, even with an SNR of −10 dB. In the middle row, where M = 8000, the performance slightly declines compared to M = 12,000, with a small offset appearing along the $\mathbf{k_x}'$ axis. Meanwhile, Figure 12c,f show similar performances to M = 8000, but in Figure 12i, there is a phenomenon of missing scatters, and the shapes of the multi-scatters are not properly reconstructed. To further evaluate the resolution capability in detail, we here analyze it by reconstructing the position error of a multi-point target with two perspectives: the number of $\mathbf{k_x}$/cross-track dimension grids and the signal-to-noise ratio of echoes. Here, the definition of reconstruction error is

$$P_{error} = \sum_{i=1}^{K} \frac{(x_i - \widetilde{x}_i)}{K} \tag{19}$$

where K denotes the number of scatters, and x_i and $\widetilde{x}_i$ represent the true $\mathbf{k_x}$ position and estimated $\mathbf{k_x}$ position, respectively. Then, we conduct 100 Monte Carlo experiments to provide a relatively clear demonstration of resolution ability, as shown in Figure 13. Regarding doubts as to why this approach is used to evaluate resolution capability, here, we will provide an explanation. The three-dimensional imaging process proposed in this paper is essentially achieved by extracting and reconstructing the target scattering point position and reflection coefficient. Therefore, we evaluate the resolution capability of the proposed algorithm by using the positioning accuracy of scattered points in three-dimensional space.

Figure 13 shows three curves, each corresponding to a different number of sampling grids. Overall, when the SNR is negative, the positioning error across all curves is relatively high. However, at an SNR of 0 dB, there is a noticeable drop in positioning error, which continues to decrease as the SNR increases. A further comparison of the curves for different sampling grids reveals that the more sampling grids there are, the smaller the positioning error becomes. This can be explained by the fact that increasing the number of sampling grids results in a finer division of the $\mathbf{k_x}$ axis space, thereby increasing the likelihood of accurately sampling the true target position. However, this also leads to a corresponding increase in computational load.

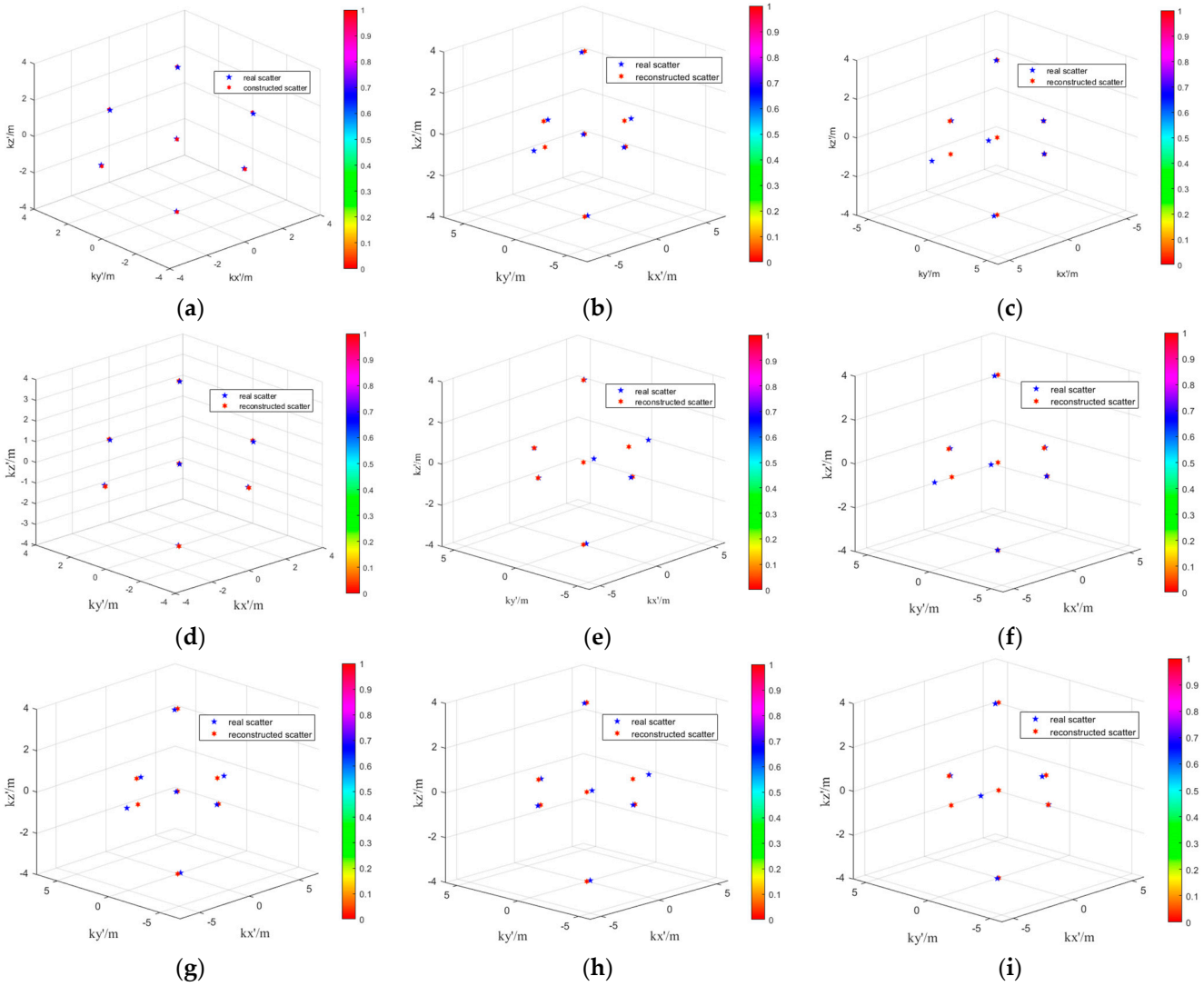

Figure 12. The effect analysis of signal-to-noise and sampling rate. (**a**) 3D imaging result with SNR = 10 dB, M = 12,000; (**b**) 3D imaging result with SNR = 10 dB, M = 8000; (**c**) 3D imaging result with SNR = 10 dB, M = 8000; (**d**) 3D imaging result with SNR = 0 dB, M = 12,000; (**e**) 3D imaging result with SNR = 0 dB, M = 8000; (**f**) 3D imaging result with SNR = 0 dB, M = 4000; (**g**) 3D imaging result with SNR = −10 dB, M = 12,000; (**h**) 3D imaging result with SNR = −10 dB, M = 8000; (**i**) 3D imaging result with SNR = −10 dB, M = 4000.

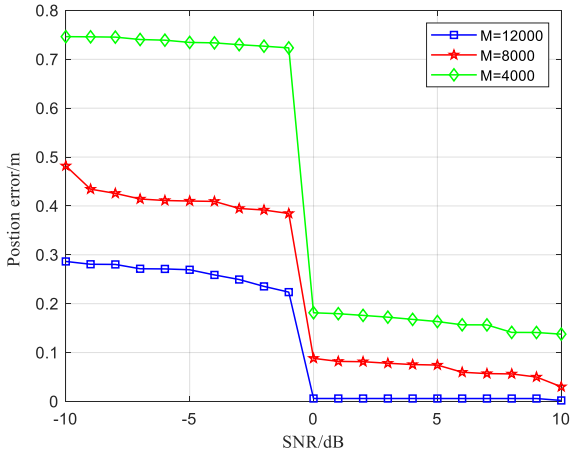

Figure 13. The $\mathbf{k_x}$ axis resolution ability analysis with the sampling grids number M and SNR.

4.3. 3D Imaging Verification with the Point Cloud Models of Actual Complex Tank Object

To further validate the practical applicability of the proposed algorithm, we selected a complex tank object for verification. The 3D imaging results are presented in Figure 14, with the sampling rate set at M = 50,000 and SNR = 10 dB. In Figure 14b, the 2D position parameters of the tank object in the $\mathbf{k_y'}$-$\mathbf{k_z'}$ focused plane are shown, where the shape of the tank is clearly discernible. The image appears clear, with sidelobes effectively eliminated, as indicated by the ample minimum value on the color bar. Figure 14c,d display the projections of the 3D imaging result in the $\mathbf{k_x'}$-$\mathbf{k_y'}$ and $\mathbf{k_x'}$-$\mathbf{k_z'}$ planes, respectively. Although a slight offset is observed, the overall shape of the tank remains identifiable. Overall, the tank object is accurately and effectively reconstructed, demonstrating the feasibility and practicality of the proposed algorithm for the 3D imaging of complex real-world objects under a maneuvering trajectory.

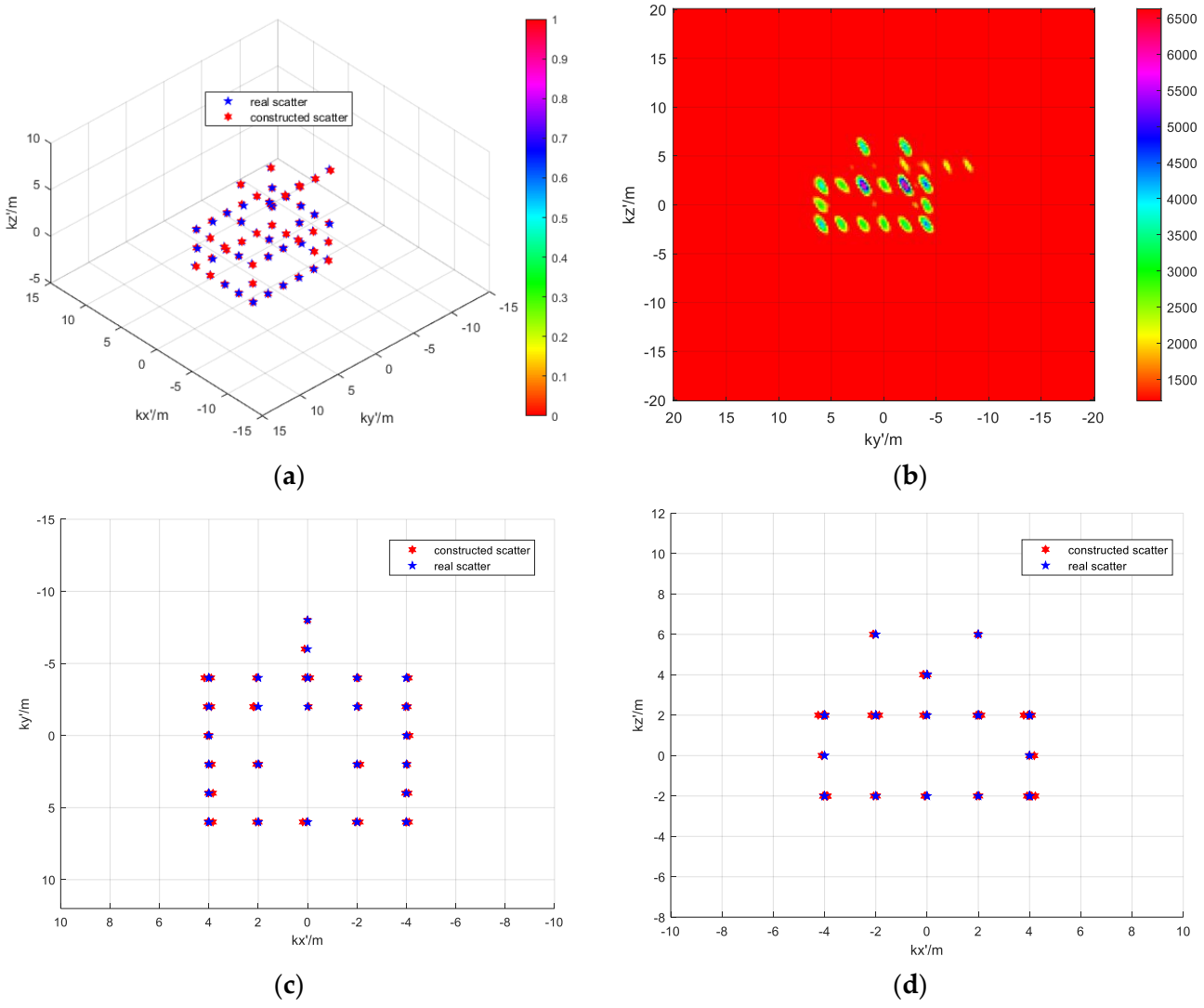

Figure 14. The 3D imaging result for an actual complex tank object. (**a**) 3D imaging result; (**b**) $\mathbf{k_y'}$-$\mathbf{k_z'}$ focused plane result; (**c**) $\mathbf{k_x'}$-$\mathbf{k_y'}$ focused plane result; (**d**) $\mathbf{k_x'}$-$\mathbf{k_z'}$ focused plane result.

5. Conclusions

Building on a comprehensive understanding of actual ballistic trajectories, this paper delves into the maneuvering trajectory characteristics of missile platforms, verifying the feasibility of 3D forward-looking imaging. This research represents a significant innovation in the field of missile technology, offering a viable technical solution for achieving forward detection in three-dimensional space.

The main contributions of this study are as follows. First, it introduces and validates the use of maneuvering trajectories for 3D forward-looking imaging—a concept not explored in the existing literature. Second, the paper provides an in-depth analysis of 3D resolution and its influencing factors, offering valuable theoretical insights that can inform future ballistic design. Finally, the study proposes a novel 3D super-resolution imaging algorithm that combines axis rotation with compressed sensing. The effectiveness and accuracy of this algorithm are validated through several rigorous experiments.

Author Contributions: Conceptualization, software and validation, writing—review and editing, T.G. and Y.G.; methodology, T.G. and Y.G.; software and validation, C.Z. and T.Z.; investigation, J.Z.; data curation, T.G.; writing—original draft preparation, T.G.; writing—review and editing, Y.G.; supervision, G.L.; funding acquisition, Y.G. All authors have read and agreed to the published version of the manuscript.

Funding: This research was supported by several foundations, including the National Natural Science Foundation of China under Grant No. 62301438 and Grant No. 62301598, the Fundamental Research Funds for the Central Universities under Grant D5000230324, and the Natural Science Basic Research Program of Shaanxi under Grant No. 2023-JC-QN-0638.

Data Availability Statement: The data presented in this study are available on request from the corresponding author. The data are not publicly available due to privacy and highly military confidential.

Conflicts of Interest: The authors declare that they have no known financial interests or personal relationships that could have appeared to influence the work reported in this paper. All authors have contributed to this research without any bias or vested interest from external entities. Furthermore, the research was conducted independently of any commercial or governmental influence. The findings and conclusions presented are solely based on scientific analysis and data, ensuring objectivity and academic integrity. The authors affirm that there are no conflicts related to the publication of this manuscript, including affiliations, financial support, or intellectual property. Any potential conflicts that could arise in the future will be promptly disclosed and addressed according to the best ethical practices.

References

1. Cumming, I.G.; Wong, F.H. *Digital Processing of Synthetic Aperture Radar Data: Algorithm and Implementation*; Artech House: Norwood, MA, USA, 2005.
2. Moreira, A.; Prats-Iraola, P.; Younis, M.; Krieger, G.; Hajnsek, I.; Papathanassiou, K.P. A tutorial on synthetic aperture radar. *IEEE Geosci. Remote Sens. Mag.* **2013**, *1*, 563–583. [CrossRef]
3. Chen, X.; Sun, G.-C.; Xing, M.; Li, B.; Yang, J.; Bao, Z. Ground Cartesian back-projection algorithm for high squint diving Tops SAR imaging. *IEEE Trans. Geosci. Remote Sens.* **2021**, *59*, 5812–5827. [CrossRef]
4. Deng, Y.; Sun, G.-C.; Han, L.; Wang, Y.; Zhang, Y.; Xing, M. 2-D Wavenumber Domain Autofocusing for High-Resolution Highly Squinted SAR Imaging Based on Equivalent Broadside Model. *IEEE Trans. Geosci. Remote Sens.* **2023**, *61*, 5220515. [CrossRef]
5. Xu, H.P.; Zhu, Y.D.; Kang, C.H.; Zhou, Y.Q. A new deramp NECS imaging algorithm for missile borne hybrid SAR. *Chin. J. Electron.* **2011**, *20*, 769–774.
6. Liu, D.; Shi, H.; Liu, H.; Yang, T.; Guo, J. Enhanced Forward-Looking Missile-Borne Bistatic SAR Imaging with Electromagnetic Vortex. *IEEE Sens. J.* **2023**, *23*, 8478–8490. [CrossRef]
7. Qian, G.; Wang, Y. Analysis of Modeling and 2-D Resolution of Satellite–Missile Borne Bistatic Forward-Looking SAR. *IEEE Trans. Geosci. Remote Sens.* **2023**, *61*, 5222314. [CrossRef]
8. Li, X.; Zhou, S.; Yang, L. A new fast factorized back-projection algorithm with reduced topography sensibility for missile-borne SAR focusing with diving movement. *Remote Sens.* **2020**, *12*, 2616. [CrossRef]
9. Wang, C.; Sun, H.; Zhang, X.-Y.; Zhang, R. A unified back-projection correction algorithm for squint SAR based on SPECAN processing. In Proceedings of the 2019 IEEE International Conference on Signal, Information and Data Processing (ICSIDP), Chongqing, China, 11–13 December 2019; pp. 1–4.
10. Tang, S.; Zhang, L.; Guo, P.; Zhao, Y. An omega-K algorithm for highly squinted missile-borne SAR with constant acceleration. *IEEE Geosci. Remote Sens. Lett.* **2014**, *11*, 1569–1573. [CrossRef]
11. Chen, S.; Zhao, H.; Zhang, S.; Chen, Y. An extended nonlinear chirp scaling algorithm for missile borne SAR imaging. *Signal Process.* **2014**, *99*, 58–68. [CrossRef]
12. Li, Z.; Xing, M.; Liang, Y.; Gao, Y.; Chen, J.; Huai, Y.; Zeng, L.; Sun, G.C.; Bao, Z. A frequency-domain imaging algorithm for highly squinted SAR mounted on maneuvering platforms with nonlinear trajectory. *IEEE Trans. Geosci. Remote Sens.* **2016**, *54*, 4023–4038. [CrossRef]

13. Zhang, Y.; Lu, C.; Zhang, H.; Li, H. A Modified CSA for Missile-Borne SAR with Curved Trajectory. In Proceedings of the 2020 IEEE Radar Conference (RadarConf20), Florence, Italy, 21–25 September 2020; pp. 1–6.
14. Saeedi, J. Feasibility study and conceptual design of missile-borne synthetic aperture radar. *IEEE Trans. Syst. Man Cybern. Syst.* **2020**, *50*, 1122–1133. [CrossRef]
15. Zhu, D.; Xiang, T.; Wei, W.; Ren, Z.; Yang, M.; Zhang, Y.; Zhu, Z. An extended two step approach to high-resolution airborne and spaceborne SAR full-aperture processing. *IEEE Trans. Geosci. Remote Sens.* **2021**, *59*, 8382–8397. [CrossRef]
16. Tang, S.; Zhang, X.; He, Z.; Chen, Z. Practical Issue Analyses and Imaging Approach for Hypersonic Vehicle-Borne SAR with Near-Vertical Diving Trajectory. *IEEE Trans. Geosci. Remote Sens.* **2023**, *61*, 5204316. [CrossRef]
17. Dong, L.; Han, S.; Zhu, D.; Mao, X. A Modified Polar Format Algorithm for Highly Squinted Missile-Borne SAR. *IEEE Geosci. Remote Sens. Lett.* **2023**, *20*, 4012905. [CrossRef]
18. Zheng, Y.; Guan, J.; Jiang, G.; Yi, W.; Yang, X.; Yin, H. A Modified Algorithm for Highly Squinted Missile-Borne SAR Imaging with Large Acceleration. *IEEE Access* **2024**, *12*, 48640–48653. [CrossRef]
19. Zebker, H.; Goldstein, R. Topographic mapping from interferometric SAR observations. *J. Geophys. Res.* **1986**, *91*, 4993–4999. [CrossRef]
20. Zhu, X.; Bamler, R. Tomographic SAR inversion by L1-norm regularization—The compressive sensing approach. *IEEE Trans. Geosci. Remote Sens.* **2010**, *48*, 3839–3846. [CrossRef]
21. Bi, H.; Zhang, B.; Hong, W.; Zhou, S. Matrix-Completion-Based Airborne Tomographic SAR Inversion under Missing Data. *IEEE Geosci. Remote Sens. Lett.* **2015**, *12*, 2346–2350. [CrossRef]
22. Reale, D.; Fornaro, G.; Pauciullo, A.; Zhu, X.; Bamler, R. Tomographic imaging and monitoring of buildings with very high resolution SAR data. *IEEE Geosci. Remote Sens. Lett.* **2011**, *8*, 661–665. [CrossRef]
23. Gu, T.; Liao, G.; Li, Y.; Liu, Y.; Guo, Y. Airborne Downward-Looking Sparse Linear Array 3-D SAR Imaging via 2-D Adaptive Iterative Reweighted Atomic Norm Minimization. *IEEE Trans. Geosci. Remote Sens.* **2022**, *60*, 5202513. [CrossRef]
24. Gu, T.; Liao, G.; Li, Y.; Guo, Y.; Liu, Y. DLSLA 3-D SAR Imaging via Sparse Recovery through Combination of Nuclear Norm and Low-Rank Matrix Factorization. *IEEE Trans. Geosci. Remote Sens.* **2022**, *60*, 5208213. [CrossRef]
25. Shao, M.; Su, C.; Zhang, Z.; Zhang, B. The application of the alternate descent conditional gradient method in tomographic SAR off-grid imaging. In Proceedings of the IET International Radar Conference (IRC 2023), Chongqing, China, 3–5 December 2023; pp. 3259–3264.
26. Tian, W.; Xie, X.; Deng, Y.; Yang, Z.; Hu, C. An Improved Imaging Method Based on Optimal Topographic Imaging Plane Reconstruction for Nonlinear Trajectory SAR. *IEEE Trans. Geosci. Remote Sens.* **2024**, *62*, 5216217. [CrossRef]
27. Meng, D.; Hu, D.; Ding, C. A New Approach to Airborne High Resolution SAR Motion Compensation for Large Trajectory Deviations. *Chin. J. Electron.* **2012**, *21*, 764–769.
28. Gorovyi, I.M.; Bezvesilniy, O.O.; Vavriv, D.M. Estimation of uncompensated trajectory deviations and image refocusing for high-resolution SAR. In Proceedings of the 2015 German Microwave Conference, Nuremberg, Germany, 16–18 March 2015; pp. 186–189.
29. Ran, L.; Liu, Z.; Zhang, T.; Li, T. Autofocus for correcting three dimensional trajectory deviations in synthetic aperture radar. In Proceedings of the 2016 CIE International Conference on Radar (RADAR), Guangzhou, China, 10–13 October 2016; pp. 1–4.
30. Ran, L.; Liu, Z.; Zhang, L.; Li, T.; Xie, R. An Autofocus Algorithm for Estimating Residual Trajectory Deviations in Synthetic Aperture Radar. *IEEE Trans. Geosci. Remote Sens.* **2017**, *55*, 3408–3425. [CrossRef]
31. Liu, Y.; Wang, W.; Pan, X.; Gu, Z.; Wang, G. Raw Signal Simulator for SAR with Trajectory Deviation Based on Spatial Spectrum Analysis. *IEEE Trans. Geosci. Remote Sens.* **2017**, *55*, 6651–6665. [CrossRef]
32. An, Z.; Xiong, F.; Li, C. A Trajectory Tracking Method Using Convex Optimization. In Proceedings of the 2020 39th Chinese Control Conference (CCC), Shenyang, China, 27–29 July 2020; pp. 3281–3287.
33. Chen, X.; Li, Z.; Yang, Y.; Qi, L.; Ke, R. High-Resolution Vehicle Trajectory Extraction and Denoising from Aerial Videos. *IEEE Trans. Intell. Transp. Syst.* **2021**, *22*, 3190–3202. [CrossRef]
34. Donoho, D.L. Compressed sensing. *IEEE Trans. Theory* **2006**, *52*, 1289–1306. [CrossRef]
35. Kim, S.-J.; Koh, K.; Lustig, M.; Boyd, S.; Gorinevsky, D. An Interior-Point Method for Large-Scale ℓ -Regularized Least Squares. *IEEE J. Sel. Top. Signal Process.* **2007**, *1*, 606–617. [CrossRef]
36. Austin, C.D.; Ertin, E.; Moses, R.L. Sparse signal methods for 3D radar imaging. *IEEE J. Sel. Topics Signal Process.* **2011**, *5*, 408–423. [CrossRef]
37. Tang, G.; Bhaskar, B.N.; Shah, P.; Recht, B. Compressed sensing off the grid. *IEEE Trans. Inf. Theory* **2013**, *59*, 7465–7490. [CrossRef]
38. Qiu, W.; Zhou, J.; Zhao, H.; Fu, Q. Three-Dimensional Sparse Turntable Microwave Imaging Based on Compressive Sensing. *IEEE Geosci. Remote Sens. Lett.* **2015**, *12*, 826–830. [CrossRef]
39. Bu, H.; Tao, R.; Bai, X.; Zhao, J. A Novel SAR Imaging Algorithm Based on Compressed Sensing. *IEEE Geosci. Remote Sens. Lett* **2015**, *12*, 1003–1007. [CrossRef]
40. Peng, X.; Tan, W.; Hong, W.; Jiang, C.; Bao, Q.; Wang, Y. Airborne DLSLA 3-D SAR image reconstruction by combination of polar formatting and L1 regularization. *IEEE Trans. Geosci. Remote Sens.* **2016**, *54*, 213–226. [CrossRef]
41. Weidner, R.J.; Mulholland, R.J. Kronecker product representation for the solution of the general linear matrix equation. *IEEE Trans. Autom. Control.* **1980**, *25*, 563–564. [CrossRef]

42. Candès, E.; Romberg, J. L-Magic: A Collection of MATLAB Routines for Solving the Convex Optimization Programs Central to Compressive Sampling 2006. Available online: www.acm.caltech.edu/l1magic/ (accessed on 7 July 2024).
43. Saunders, M. PDCO: Primal-Dual Interior Method for Convex Objectives 2002. Available online: https://github.com/mxsaunders/pdco (accessed on 5 September 2024).
44. Hager, W.W.; Zhang, H. A survey of nonlinear conjugate gradient methods. *Pac. J. Optim.* **2006**, *2*, 35–58. [CrossRef]
45. Paige, C.; Saunders, M. LSQR: An algorithm for sparse linear equations and sparse least squares. *ACM Trans. Math. Softw.* **1982**, *8*, 43–71. [CrossRef]